Additive Manufacturing of Alumina Components by Extrusion of *in-situ* UV-cured Pastes

Lok-kun Tsui*, Erin Maines†, Lindsey Evans†, David Keicher@, and Judith Lavin†

*Center for MicroEngineered Materials, University of New Mexico, NM 87106
†Advanced Materials Laboratory, Sandia National Laboratories, NM, 87106
@Integrated Deposition Solutions, Inc. NM, 87110

Abstract

Additive manufacturing of ceramic materials is an attractive technique for rapid prototyping of components at small scales and low cost. We have investigated the printing of alumina pastes loaded at 70-81.5 wt% solids in a UV curable resin. These can be deposited by extrusion from a syringe head on a Hyrel System 30M printer. The print head is equipped with an array of UV LEDs, which solidify the paste without the need for any applied heating. Parameters optimized include print speed, layer height, applied force, and deposition rate. Using A15 alumina and submicron A16 powder precursors, we can achieve bulk densities of 91% and 96% of theoretical density respectively. The influence of dispersants and surfactants added to the powder on the rheology of the pastes, the print process parameters, and the quality of the final components are also investigated.

Introduction

Additive manufacturing of ceramic components enables the prototyping of materials and processes at small scales and in geometries difficult to produce with conventional ceramic fabrication techniques [1]. This technique has been used in applications for structural ceramics, biologically compatible components, electronics, and chemical sensors.[1–6] Processes available for additive manufacturing of ceramics include robocasting,[7] where a paste containing ceramic powder and an aqueous or organic binder is extruded from a computer controlled printer onto a heated substrate; freeze form extrusion fabrication, where a paste is extruded onto a cold surface and frozen in place [8]; and stereolithographic printing where a slurry of material is exposed to a 2D pattern of light produced by a projector [4,9,10]. An alternative to these techniques combines the use of light-curable pastes with extrusion by using a UV-light source to cure the pastes as they are being printed. This allows the use of small quantities of material in cases where materials are expensive or scarce and the light source removes the need for a heating or cooling system for solidification. Faes et al. have investigated the extrusion of UV-curable pastes with zirconia and achieved 92% theoretical density [11,12].

We report on the printing of UV-curable pastes containing alumina powders from a commercially available extrusion printer, including the modifications made to the printer in order to monitor the force applied during deposition. Paste composition, printing parameters, and heat treatment conditions were optimized to maximize the final sample density. We are able to achieve up to 90-92% and 94-96% of theoretical alumina bulk density using A15 and A16 alumina

precursors respectively. It is necessary to understand where the defects, which cause deficiencies in final density, are located. Electron microscopy in principle allows the imaging of defects of printed parts, but imaging is limited to only the surface or the sample must be sectioned destructively to evaluate the interior structure. On the other hand, x-ray computed tomography imaging is a technique used to non-destructively visualize the location and distribution of defects inside these parts.

Experimental Section

A16 and A15 alumina powders were obtained from Almatis with the peak of the particle size distribution being 0.5 µm for A16 and a bimodal distribution in A15 with peaks at 0.5 µm and 4 µm. The powders were prepared by ball milling with 5 mm yttria-stabilized zirconia beads in either ethanol with 0.5 wt% oleic acid or toluene with 2 wt% Hypermer KD1 dispersant. After milling, the solvent was allowed to evaporate at room temperature and then the powders dried in a drying oven at 80ºC overnight. The dry powder was then crushed with a mortar and pestle and sieved using a No. 40 sieve (425 µm mesh).

Pastes were prepared using Tethon3D Genesis UV-curable resin with a Thinky centrifugal planetary mixer. For each batch of paste, the alumina was added into the resin in 1/3 size batches and mixed at 2000 RPM for 1 minute at ambient atmospheric pressure. The completed paste was then loaded into a 5 mL syringe and centrifuged at 2500 RPM for 1 minute. Finally, the syringe was placed into the Thinky planetary mixer and mixed again at 2000 RPM under 7 kPa vacuum to degas the paste. Paste loading was varied between 71-82 wt% alumina. A table of pastes evaluated in this set of experiments is shown in Table 1.

The printing was performed using a Hyrel System 30M 3D printer which can accept a variety of heads including traditional fused deposition modeling printing of plastic components and extrusion of slurries and pastes from a syringe head. We have modified the CSD-05 syringe head with a force sensor (Omega LCFL-75 coupled with a DMD4059-DC signal conditioner and amplifier). The signal is received with a National Instruments DAQmx USB-6218 controlled by LabVIEW. A schematic of the force sensing system is shown in Figure 1(a) and a photograph of an unmodified syringe head is shown in Figure 1(b). The Hyrel System 30M may be controlled by standard GCODE generated from 3D printing slicer software such as the included Slic3r or Ultimaker Cura. For the results reported here, we used Ultimaker Cura v. 3.0.2 to generate toolpaths. The CSD-05 head includes three 365 nm UV LEDs which operate at a power density of 0.25-0.5 W/cm^2 during printing. Jensen Global opaque Luer lock syringe tips with nozzle diameter 0.025" (635 µm) was used for all printing experiments. Glass microscope slides (75 x 50 x 1 mm) were used as substrates. A list of other printing parameters is shown in Table 2. Simple geometric structures were chosen for testing including a 7.5 x 7.5 x 7.5 mm cube, a 7.5 mm diameter x 7.5 mm height cylinder, and a ring with 8.0 mm outer diameter, 4.8 mm inner diameter, and thickness of 4.6 mm. After the components were printed they were exposed to high intensity UV-LED radiation from a Phoseon UV light source with a power density of 300 W/cm^2. Samples underwent burnout and sintering in air and the heat treatment parameters are shown in Table 3. Heat treatment processes were performed in Carbolite CWF 12/5 and Deltech DT-37FL-10-E3504 box furnaces for burnout and sintering respectively.
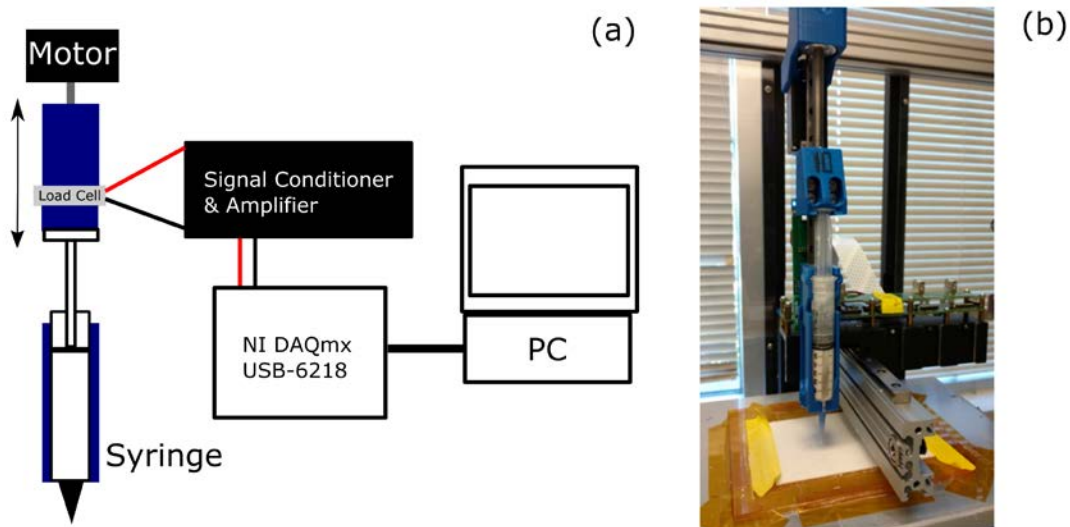
Figure 1. (a) Schematic of the syringe head modified with a load cell and signal conditioner to perform force measurements as a function of time. (b) A photograph of the syringe print head is shown.

Paste Name	Alumina Type and Loading	Oleic Acid	Hypermer KD1	Genesis Resin
A15G81.5	A15 81.5 wt%	0.4 wt%	0 wt%	18.1 wt%
A16G71	A16 71.0 wt%	3.6 wt%	1.4 wt%	24.0 wt%
A16G73	A16 73.0 wt%	3.7 wt%	1.5 wt%	21.8 wt%
A16G77	A16 77.0 wt%	3.8 wt%	1.5 wt%	17.7 wt%
A16G80	A16 80.0 wt%	4.0 wt%	1.6 wt%	14.4 wt%
A16G82	A16 82.0 wt%	4.1 wt%	1.6 wt%	12.3 wt%

Table 1. Paste compositions studied for printing. All values shown are wt% with respect to total paste mass.

Parameter Name	Value
Extrusion Multiplier[A]	0.2
Layer Height	200 μm
Computed Line Width	200 μm
Infill	90%
Top and Bottom Layers	Disabled
Printing Substrate Temperature	Room Temperature (22°C)
Printing Speed	4 mm/s outer perimeter, 7 mm/s infill
Travel Speed	17 mm/s

Table 2. Printing Parameters for deposition of alumina pastes with the Hyrel System 30M. [A]Extrusion multiplier – unitless tuning factor in the Hyrel control software for flow rate.

Temperature (ºC)	Ramp Rate (ºC/min)	Hold Time (Hours)
Burnout (Air atmosphere)		
225	0.5	0.5
625	0.5	1.0
1000	1.0	1.0
25	-3.0	0.0
Sintering (Air atmosphere)		
1625	3.0	2.0
25	-5.0	0.0

Table 3. Heat treatment parameters for burnout and sintering for alumina components.

The as-deposited and post-heat treatment geometry of the samples were measured by optical microscopy using a Keyence Optical Microscope. Density measurements of the components were performed using the Archimedes technique in DI water and compared with the theoretical density of alumina (3.99 g/cm^3 [13]). X-ray tomography was obtained on the samples using a North Star Imaging industrial microfocus CT instrument with 150 keV x-rays and imaging pixel resolution of 8.3 μm. Rheological measurements of the paste were performed with a Haake Mars 2 35 mm cone-plate rheometer at 1 degree. An initial constant stress was of 3000 Pa was applied for 120 seconds and the paste was allowed to equilibrate for 500 seconds. A shear rate sweep was performed from 0.11 Hz to 1000 Hz.

Results and Discussion

1. Paste Rheology and Force Monitoring

Initial sets of tests to determine rheological properties, applied force during printing, and print accuracy and force as a function of time were performed on pastes consisting of 81.5 wt% A15 alumina (A15G81.5 in Table 1). Rheological properties of the paste are shown in Figure 2(a) for three sequential runs. The paste exhibit shear thinning behavior, which is desirable for an extrusion application. The paste should be self-supporting when no force is applied and flow easily when sheared in the syringe. We observe hysteresis in the scans with the return scan showing lower viscosity than the onset scan. Figure 2(b) shows the force as a function of time for constant flow of material at a dispensing rate of 1.1 μL/s. In the first 30 seconds after the dispense head contacts the syringe plunger, the force rises linearly until material begins to extrude from the nozzle. The force then reaches a steady state of 45N (200-350 seconds). Dispensing was stopped at 350 seconds and we observe a decay to a resting force of 30N as material continues to be extruded even after motorized dispensing is stopped. This resting force corresponds to the minimum force necessary for the paste to flow out of the syringe nozzle. The addition of the force measurement device to the 3D printer allows real-time monitoring of the applied force during printing to verify whether the material is being consistently extruded. Motor belt skipping can also be detected by watching for sudden decreases in applied force. This occurs when the necessary torque needed to extrude more material exceeds what the stepper motor in the Hyrel CSD-05 head can supply.

The print speeds and extrusion factor shown in Table 2 were the result of adjustments so that continuous layers were deposited for the cubes and cylinders. An excessive extrusion factor

or slower print speed results in over-extrusion and loss of resolution, while too small of an extrusion factor or too fast of a print speed results in under extrusion and leaves large voids in the structure. We determined that the smallest height that we could consistently print structures with was 200 μm, as any smaller would require extrusion rates too which corresponded to applied forces too small to induce material flow from the nozzle.
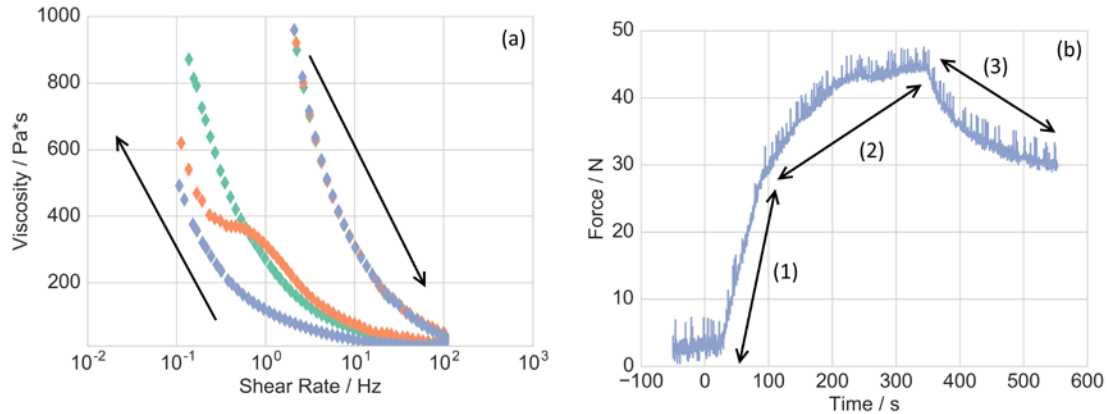

Figure 2. (a) Viscosity vs. shear rate of 81.5 wt% A15 in Genesis showing three sequential scans. Arrows indicate the direction of onset and subsequent return scans. (b) Force curve for this paste with a constant dispensing rate with showing three distinct regions corresponding to onset (1), steady-state (2), and decay to idle force (3) after dispensing is stopped at 350 seconds.

2. Print Accuracy

3D models and optical microscopy of some simple geometric structures are shown in Figure 3 and a comparison of the expected parameters and the printed parameters are collected in Tables 4 and 5. The axes conventions used are as follows: Z represents the direction perpendicular to the substrate, while X and Y represent directions in parallel to the substrate. The average sizes of the as deposited structures are typically within 100 μm of the target structure. The main aspects of the printer and print head which impose limitations on resolution are the layer step height of 200 μm and the nozzle diameter of 635 μm. The samples exhibit a higher shrinkage in the Z direction due to the greater density of voids that are eliminated in that direction during sintering. The bottom surface tends to be smooth since it is in contact with the glass substrate during printing while the top surface shows roughness due to the printing of lines which are not spread out against a substrate. If smoothness is desired, the components in their green state may be polished with 1000, 1500, and 2500 grit polishing paper.

Parameter Name	Nominal	As Deposited	Final Sintered
Length (X)	7.5 mm	7.50 mm (±0.09 mm)	6.37 mm (±0.03 mm)
Width (Y)	7.5 mm	7.54 mm (±0.15 mm)	6.35 mm (±0.19 mm)
Height (Z)	7.5 mm	7.51 mm (±0.08 mm)	6.10 mm (±0.08 mm)
Aspect Ratio	1.0	0.999 (±0.01)	0.959 (±0.01)
Length Shrinkage (X)			15%
Height Shrinkage (Z)			19%
Volumetric Shrinkage			42%
Final Density (% of Theoretical)			91.51% (±0.5%)

Table 4. Nominal geometric parameters, as-deposited measurements and post-sintering measurements of the 7.5 mm cube structures. The numbers in parentheses represent standard deviation of 6 samples for as deposited parts and 5 samples for sintered parts.

Parameter Name	Nominal	As Deposited	Final Sintered
Diameter (X,Y)	7.5 mm	7.49 mm (±0.06 mm)	6.59 (±0.03 mm)
Height (Z)	7.5 mm	7.44 mm (±0.06 mm)	6.07 (±0.04 mm)
Aspect Ratio	1.0	0.993 (±0.01)	0.920 (±0.01)
Diameter Shrinkage (X,Y)			12%
Height Shrinkage (Z)			18%
Volumetric Shrinkage			37%
Final Density (% of Theoretical)			90.39% (±1.4%)

Table 5. Nominal geometric parameters, as-deposited measurements and post-sintering measurements of the 7.5 mm diameter x 7.5 mm height cylinder structures. The numbers in parentheses represent standard deviation of 6 samples for as deposited parts and 5 samples for sintered parts.
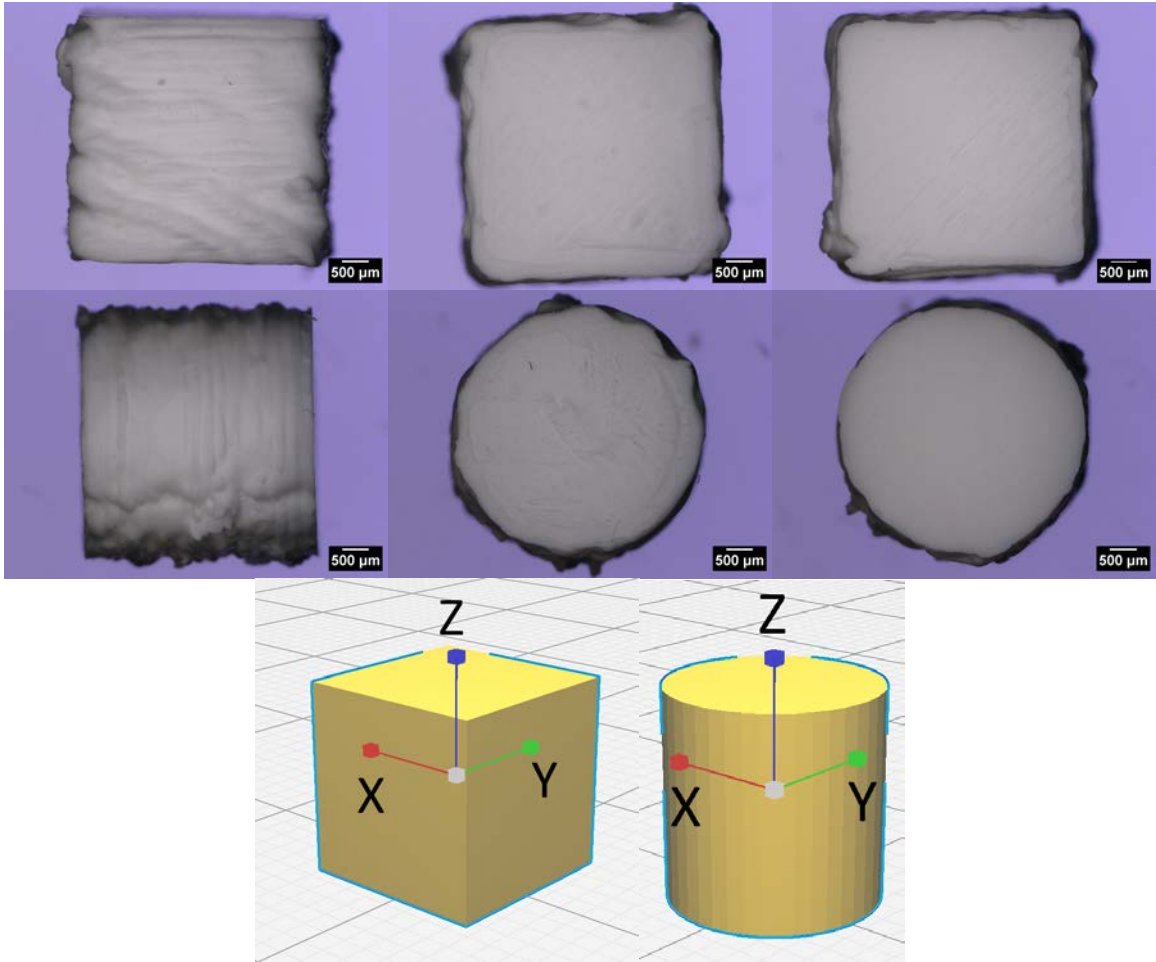
Figure 3. Optical microscopy of post-sintered (top row) Cube and (middle row) cylinder. The images show the samples in different views: (left) Side view. (center) Top view. (right) Bottom view. 3D models of the test structures are shown on the bottom row with the axes convention.

3. Component Density and Internal Defects

The density of the components created with A15 is only about 90-92% of theoretical alumina density. Per specifications received from the manufacturer, A15 contains a bimodal distribution of particle sizes peaked at 0.5 µm and 4 µm. The larger particles in this powder have lower surface area compared to that of A16, and therefore the driving force for sintering is weaker. To remedy this we moved to using A16 alumina with a unimodal particle size distribution with a peak at 0.5 µm. The smaller particle size produces a mixture with higher viscosity, necessitating the use of dispersants. With only OA, the maximum loading that could be extruded on our printer is 71 wt%. The introduction of Hypermer KD1 in place of oleic acid at loadings of 2 wt% KD1 resulted in a mixture with a consistency of water up to 82% where a transition to a shear thickening material occurs. This behavior was observed qualitatively by disturbing the paste with a wooden spatula. In the presence of both 5 wt% OA and 2 wt% KD1 the paste is a shear thinning material, which can be extruded at loadings up to 82 wt% (Pastes A16G71 to A16G82 in Table 1). The oleic acid acts as a lubricant so that the particles can slide past each other. Otherwise, the particles jam together during the application of a shear force, resulting in shear thickening behavior.

Experiments conducted using A16 used the 8.0 mm diameter ring structures to determine shrinkage and theoretical density. Components printed using 71 wt% A16, without accounting for shrinkage, exhibited a maximum theoretical density of 96%. The next set of experiments investigated the influence of powder loading between 71 and 82wt% on the density and shrinkage of the samples. Microscopy of a ring structure printed with 82 wt% A16 is shown in Figure 4. In this set of samples, the components were printed with a linear scaling factor of 1.26 to 1.39x to compensate for shrinkage during sintering based on the expected volumetric shrinkage from the loading of the powders. Figure 5 shows trends in the final post-sintered density as a function of sample loading of the components determined using the Archimedes technique. In the range of loadings tested, the density increases from 88% to 95% of theoretical density. The reason that the 71 wt% sample has a lower density than the initial test, which achieved 96%, is that the larger components have been scaled for shrinkage requiring more layers, and therefore, contain a greater number of defects. We also observe a decrease in the fraction of open pores with higher loadings—this is due to less surface cracking when less shrinkage occurs in higher loading samples. An increase in the fraction of closed pores is observed with increasing loading. This may be a result of the high viscosity of the paste preventing it from easily flowing into and filling internal voids. Figure 5(c) shows trends in the shrinkage as the alumina solids loading is increased. In all cases, the shrinkage in the Z-thickness of the rings is greater than the thickness in the X-Y direction, indicating that shrinkage compensation must be greater in the Z direction than the X-Y direction. The shrinkage for thickness, outer diameter, and volumetric shrinkage is observed to decrease linearly with increasing alumina solids loading.
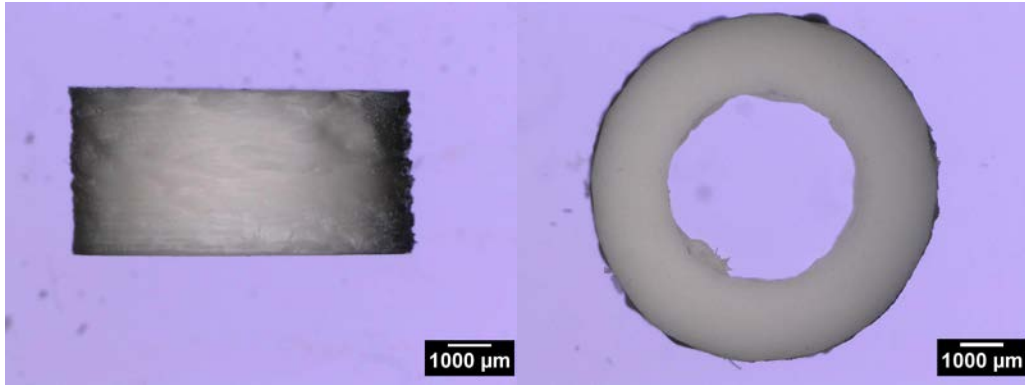
Figure 4. Side view and top view of an alumina ring structure printed with A16 alumina after sintering.
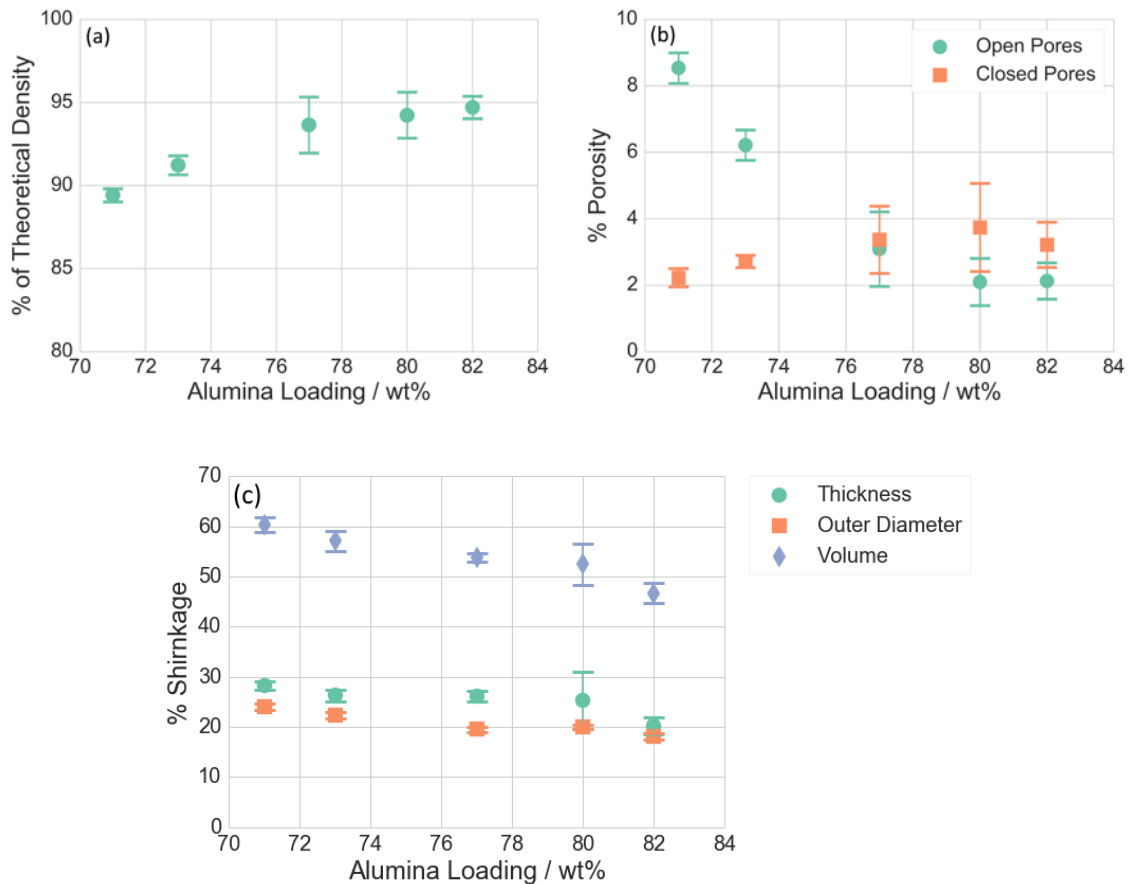

Figure 5. (a) Fraction of theoretical density as a function of alumina loading shows an increase in the density of the components. (b) The fraction of open pores decreases as a function of alumina loading while the fraction of closed pores increases. (c) Shrinkage as a function of alumina solids loading decreases linearly in for both length parameters and volumetric shrinkage. Error bars represent standard deviation of 6 samples.

4. X-ray Computed Tomography

Finally, X-ray tomographic imaging is used to non-destructively probe for detects in the interior of additively manufactured ceramics. Cross sections in the X-Y and X-Z planes of the ceramic cylinders are shown in Figure 6. Dark areas represent voids, while light areas represent solid material. The x-ray imaging indicates small cracks embedded inside the alumina structure, which are responsible for the deficiency in density. In the X-Y plane, defects are located close to the outer edges of the ring structure. In the X-Z plane, the defects are located in lines parallel to the plane of the layers during printing. This indicates that one source of defects is the deposition of layers on top of each other inducing the formation of voids at the interface. Careful tuning of the deposition parameters will be needed in order to minimize void formation between the layers.
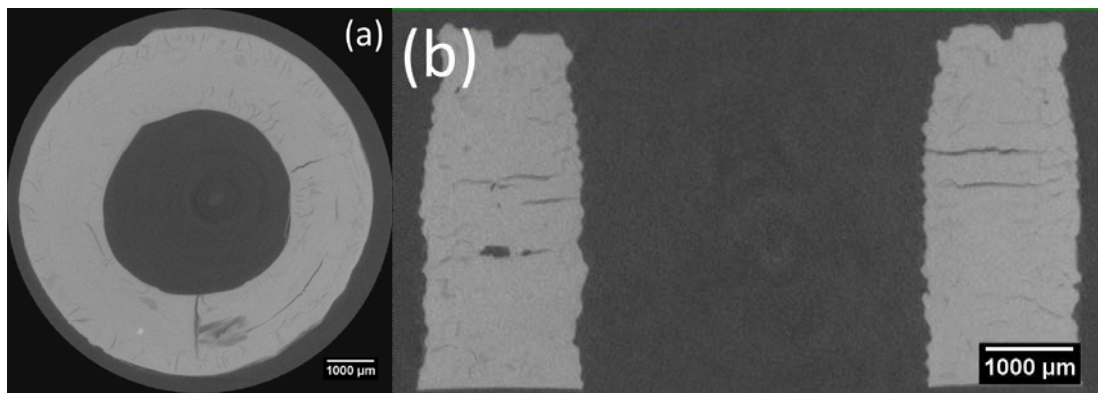

Figure 6. X-ray computed tomography of an A16 ring structure. (a) Cross section through a ring structure in the X-Y plane and (b) cross section through a ring structure in the X-Z plane.

Conclusions

We have studied the use of UV-curable alumina pastes to additively manufacture ceramic components. The rheology and force as a function of time for a constant dispensing rate of the pastes were examined. The geometry and final sintered density of the printed components was measured, and higher densities were observed by using smaller particle size alumina precursors allowing us to reach a maximum density of 95-96% of the theoretical density of alumina. X-ray tomography was then used to visualize the location and distribution of defects which contribute to deficiencies in component density.

Acknowledgements

References

[1]   N. Travitzky, A. Bonet, B. Dermeik, T. Fey, I. Filbert-Demut, L. Schlier, T. Schlordt, P. Greil, Adv. Eng. Mater. 16 (2014) 729–754.

[2]   P. Sarobol, A. Cook, P.G. Clem, D. Keicher, D. Hirschfeld, A.C. Hall, N.S. Bell, Annu. Rev. Mater. Res. 46 (2016) 41–62.

[3]   I. Denry, J.R. Kelly, J. Dent. Res. 93 (2014) 1235–1242.

[4]   Z.C. Eckel, C. Zhou, J.H. Martin, A.J. Jacobsen, W.B. Carter, T.A. Schaedler, Science (80-.). 351 (2016) 58–62.

[5]   L. Tsui, A. Benavidez, L. Evans, F.H. Garzon, Prog. Addit. Manuf. (2018).

[6]   L. Ferrage, G. Bertrand, P. Lenormand, D. Grossin, B. Ben-Nissan, J. Aust. Ceram. Soc. 53 (2017) 11–20.

[7]   J. Cesarano, MRS Proc. 542 (2011) 133–139.

[8]   T. Huang, M.S. Mason, G.E. Hilmas, M.C. Leu, Virtual Phys. Prototyp. 1 (2006) 93–100.

[9]   E. Johansson, O. Lidström, J. Johansson, O. Lyckfeldt, E. Adolfsson, Materials (Basel). 10 (2017) 138.

[10]   R. Felzmann, S. Gruber, G. Mitteramskogler, P. Tesavibul, A.R. Boccaccini, R. Liska, J. Stampfl, Adv. Eng. Mater. 14 (2012) 1052–1058.

[11]   M. Faes, H. Valkenaers, F. Vogeler, J. Vleugels, E. Ferraris, Procedia CIRP 28 (2015) 76–81.

[12]   M. Faes, J. Vleugels, F. Vogeler, E. Ferraris, CIRP J. Manuf. Sci. Technol. 14 (2016) 28–34.

[13]   W.H. D. Lide, ed., in:, CRC Handb. Chem. Phys., 94th ed., Taylor and Francis Group, LLC, Boca Raton, FL, 2014, pp. 4–38.